

Determining the defect density of states by temperature derivative admittance spectroscopy

Jian V. Li^{a)} and Dean H. Levi

National Renewable Energy Laboratory, Golden, Colorado 80401 USA

(Received 30 June 2010; accepted 8 March 2011; published online 18 April 2011)

We demonstrate that the temperature derivative admittance spectroscopy method can be used to directly determine the defect density of states. The density of defect states is proportional to the temperature derivative of the capacitance. This method is equivalent to the existing frequency derivative method in principle but possesses certain key advantages for detection of deep levels. To illustrate these advantages, we define the activation energy of a fictitious defect the Arrhenius plot of which extends diagonally across the measurable temperature-frequency range. Below this level (that is, shallower defects), the frequency derivative method is advantageous, and above this level (that is, deeper defects), the temperature derivative method is advantageous. The temperature derivative method allows a wider observation window of defect energy that avoids possible detection failure and facilitates simultaneous observation of multiple defects. For deep defects, it also yields more Arrhenius plot data points and therefore enables more accurate extraction of defect energy and capture cross-sections. In general, the temperature derivative method can avoid system noise at low frequency and is relatively immune to baseline effects due to parasitic circuit effects. © 2011 American Institute of Physics. [doi:10.1063/1.3573538]

I. INTRODUCTION

Admittance spectroscopy¹ has been an effective tool for the study of the electrical properties of defects in semiconductors. In thin film solar cell research, the use of this technique is particularly extensive² because defects are a primary limiting factor of solar cell performance. An electrically active defect reveals itself as a peak in the conductance G versus temperature T or G/ω versus frequency ω curves and as a step in the capacitance C versus T or C versus ω curves. In the early days of admittance spectroscopy, the peak temperatures of the iso-frequency G versus T curves (or peak frequencies from the iso-thermal G/ω vs ω curves) were plotted against the corresponding measurement frequencies (temperatures) in an Arrhenius plot. A line fitting then yields the activation energy (E_a) and pre-exponential factor (v_0) according to the Arrhenius equation: $\omega = v_0 \exp(-E_a/k_B T)$. It is less common to use the C versus ω curve for the acquisition of the Arrhenius plot data because the step transition is not as easy to identify. Differentiation of C with respect to frequency yields peak features, but it had been technologically challenging because the capacitance data were acquired only at a few discrete frequencies, that is, until instruments capable of continuous frequency scanning such as impedance analyzers became available. A relation between the defect density of states and the frequency derivative of capacitance $\omega dC/d\omega$ versus ω was further derived by Walter *et al.*³ and has since been widely adopted.

On the other hand, Tan and Xu⁴ proposed using the temperature derivative dC/dT versus T , but there have been few experimental works on this. In this work, we investigate the temperature derivative admittance spectroscopy technique

beyond Tan and Xu's⁴ work to extend its capability. First we establish the feasibility of using this method to determine the defect distribution in energy. We then discuss the equivalency between the temperature and frequency derivative methods in the context of the generalized temperature-rate duality. We apply both methods in observation of a defect with Gaussian density of states and compare their performance under practical experimental settings. Specifically, we inspect the observable energy window, immunity to baseline and noise, and productivity of Arrhenius plot data. The temperature derivative method is superior to its frequency derivative predecessor in most of these aspects. We use experimental data taken from GaAs solar cells for this comparison.

II. THEORY

Admittance spectroscopy probes the electrical properties of defects in the bandgap by measuring the junction current in response to small signal sinusoidal voltage stimulus. The complex transfer function consists of real (conductance) and imaginary (capacitance) parts, which are both functions of temperature and frequency. The voltage stimulus modulates the band bending, making it possible for the defects that intersect with the quasi-Fermi level to be emptied and filled periodically. However, not all such defects can exchange carriers with the majority carrier band. The capture and emission dynamics determines that for a particular temperature and frequency, only those defects the energy of which is less than the demarcation energy:

$$E_\omega = k_B T [\ln(2v_0) - \ln(\omega)], \quad (1)$$

where k_B is the Boltzmann's constant and v_0 is the pre-exponential factor, can respond to the voltage stimulus and

^{a)}Author to whom correspondence should be addressed. Electronic mail: jian.li@nrel.gov.

contribute to the measured admittance. We will focus on processing of capacitance data in this work because the same information regarding the defect is contained in both the conductance and the capacitance data due to the Kramers-Kronig relationship.⁵

In Losee's original paper¹ and a more detailed study by Cohen and Lang,⁶ the admittance due to defect levels is obtained by numerically solving Poisson's equation. This method is rigorous in physics, but it is not simple to use. An alternative approach is to use the equivalent circuit model.⁴ This method is simple and easy to use but loses some physics such as the detailed information related to the density of states. Barbolla *et al.*⁷ applied small signal analysis to carrier capture and emission rate equations to arrive at an expression for the complex admittance. Walter *et al.*³ used the rate equation approach to further derive a simple relation between the defect density of states and the normalized frequency derivative of capacitance $\omega dC/d\omega$ versus ω . We adopt this approach in this work to determine the density of states from the temperature derivative of the capacitance. Assuming the same device structure and related approximations as Walter *et al.*, we begin with rewriting Eq. (21) from Ref. 3,

$$C = -\frac{q}{\hat{u}_{\text{ext}}} \int_{E_\omega}^{E_{fp\infty}} \hat{u}_p N_t(E) \frac{w}{U_d} dE, \quad (2)$$

where $E_{fp\infty}$ is the position of the Fermi level in the bulk *p*-type semiconductor, \hat{u}_{ext} the amplitude of the external bias modulation, \hat{u}_p the local shift of quasi-Fermi level in the *p*-type semiconductor, $N_t(E)$ is the defect density of states, w the depletion width, U_d the built-in field, and q the elemental charge. Walter *et al.*³ took the derivative of C with respect to ω to arrive at the relation between $N_t(E)$ and $\omega dC/d\omega$ [Eq. (23) in Ref. 3]:

$$N_t(E_\omega) = -\frac{U_d}{qw k_B T} \omega \frac{dC}{d\omega}, \quad (3)$$

where the approximation $\hat{u}_{\text{ext}} = \hat{u}_p = \text{constant}$ has been used. For temperature derivative admittance spectroscopy, we instead take the derivative of C with respect to T :

$$\frac{dC}{dT} = \frac{dC}{dE_\omega} \frac{dE_\omega}{dT} = k_B [\ln(2v_0) - \ln(\omega)] \frac{dC}{dE_\omega}, \quad (4)$$

where $dE_\omega/dT = k_B [\ln(2v_0) - \ln(\omega)]$ has been used. Eqs. (2) and (4) yield the density of states as:

$$N_t(E_\omega) = -\frac{U_d}{k_B q w} \frac{1}{\ln(2v_0) - \ln(\omega)} \frac{dC}{dT}, \quad (5)$$

where the term before dC/dT is a slowly varying function of temperature specific to the device structure. To a good approximation, one can regard it as a constant. Therefore the density of states is directly proportional to the temperature derivative of the capacitance dC/dT . We note that Eqs. (3) and (5) are good approximations for the *nip* device structure and may be modified with minor algebra for other device structures.

The reason that frequency and time domain analysis arrive at the same physics is the fundamental T - ω duality, which was first discussed in deep level transient spectroscopy by Agarwal *et al.*⁸ Due to the Arrhenius equation, ω and T are not independent quantities in a process with definite activation energy E_a and pre-exponential factor v_0 . This is evident⁹ in the rearranged form of Eq. (1):

$$T = E_\omega / k_B [\ln(2v_0) - \ln(\omega)]. \quad (6)$$

In a previous work,⁹ we investigated the duality relation in a general activated process and developed the two-dimensional Arrhenius plot method to extract the activation energy and pre-exponential factor local to a particular $(\omega_{\text{fix}}, T_{\text{fix}})$ point. The frequency derivative admittance spectroscopy data $\omega dC(\omega, T)/d\omega$ was used there as an example of an arbitrary function $X(\omega, T)$ dependent on both ω and T , which can be separated into the iso-thermal $X(\omega, T=T_{\text{fix}})$ and iso-rate $X(\omega=\omega_{\text{fix}}, T)$ functions agreeing with each other near the intersection point $(\omega_{\text{fix}}, T_{\text{fix}})$. Obviously C is also a qualified function satisfying the duality relationship. Furthermore, differentiation of the rearranged Arrhenius equation [Eq. (6)]

$$dT = \frac{E_\omega}{k_B [\ln(2v_0) - \ln(\omega)]^2} d\ln(\omega) \\ = \frac{T}{\ln(2v_0) - \ln(\omega)} d\ln(\omega) \quad (7)$$

leads to the fact that the differentiation operations are equivalent to each other except for a proportional factor consisting of fixed T [or $\ln(\omega)$] in the respective frequency (or temperature) scan. The arrival to the same defect density of states by both the temperature and frequency derivative methods is a manifestation of the general temperature-rate duality, albeit in the differential form.

III. EXPERIMENT

Admittance spectroscopy in the frequency range of interest is traditionally measured by the bridge method or the lock-in method. The lock-in method offers improved signal-noise ratio, but the maximum accessible frequency is generally limited to about 100 kHz, which limits the low end of the observable energy. The admittance measurement is usually performed at a fixed reference frequency, but frequency scanning can also be realized via custom programming. Earlier bridge-method-based capacitance meters only function at fixed frequencies. The lack of a frequency scanning capability poses difficulties for data processing such as numerical differentiation. Modern impedance analyzers, which are used in the majority of the recent work, employ advanced techniques such as the auto-balancing bridge method¹⁰ and are capable of continuous scanning over a wide frequency range. The frequency accuracy and resolution, on order of 10^{-6} , enables frequency scans up to thousands of points. Due to the series resistance and parasitic inductance,¹¹ many admittance spectroscopy experimental setups have a high frequency limit (usually below 1 MHz). On the other hand, system noise becomes prevalent at the low frequency end (less than 1 kHz) because the admittance of a capacitor

scales with frequency. This is where a lock-in amplifier may outperform the impedance analyzer. In this work, we use an Agilent 4294A impedance analyzer to measure the admittance data. Unless otherwise mentioned, we use a 100-point logarithmic frequency scan over 100 Hz to 1 MHz.

The other half of the experimental setup concerns temperature control and monitoring. We use a closed-cycle cryostat to house the sample. The temperature is measured by one temperature sensor (A) located at the cold finger and used by the control electronics in the temperature controller (Lakeshore 311). Because many samples have a thermally insulating substrate such as glass, the actual temperature can be very different (by as much as 30–40 K) from that measured by sensor A. We therefore read sample temperature from a second temperature sensor (B) attached directly to the top of the sample. The accuracy of the temperature sensor (Lakeshore silicon diode DT-670-SD) is limited to ± 0.5 K. We set the temperature step size to be 10 K between 80 and 330 K.

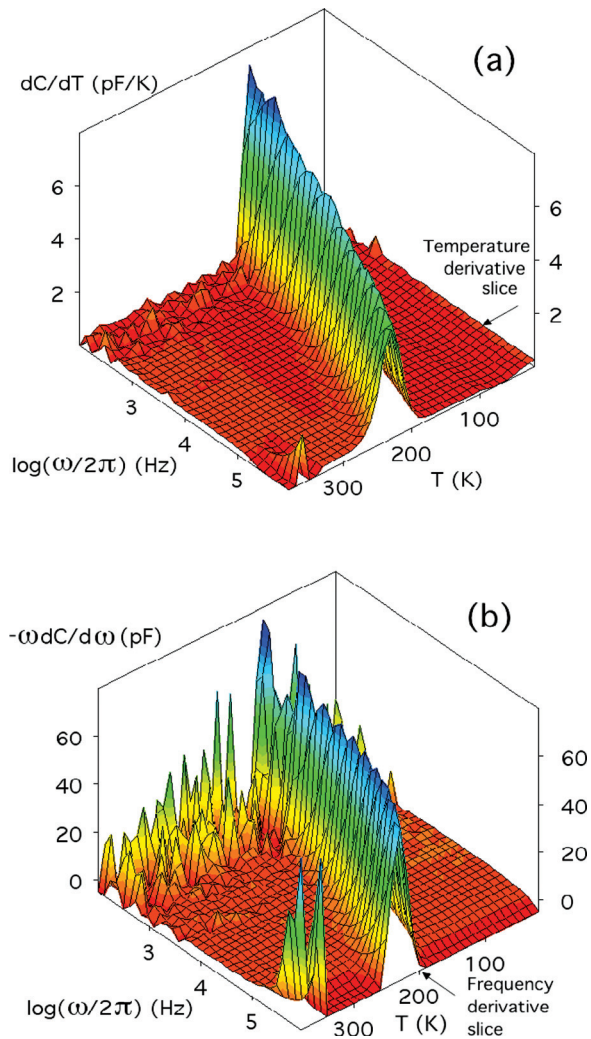


FIG. 1. (Color) Two-dimensional surface of dC/dT (a) and $\omega dC/d\omega$ (b) plotted in the T - ω plane. The data are taken from a GaAs solar cell. The arrows indicate how the frequency derivative ($\omega dC/d\omega$ vs ω) and temperature derivative (dC/dT vs T) curves are generated via slicing the two-dimensional surfaces along the ω and T axes at fixed temperature and frequency, respectively.

The preceding experimental conditions are typical and representative of those reported in recent publications. We use the same frequency and temperature range and scanning settings for simulation of admittance spectroscopy data. The experimental admittance data are taken in a matrix scanning fashion: after the cryostat is stabilized at each setting temperature, the capacitance is measured in one frequency scan. In the end, one gets a two-dimensional array of raw $C(\omega, T)$ data, from which the derivative data are generated via numerical differentiation with respect to the respective variables. The GaAs solar cell samples used in this study are grown under nonoptimized conditions by molecular beam epitaxy. The active area of the devices is 1 mm².

IV. RESULTS AND DISCUSSIONS

A. Experimental

We plot the $dC(\omega, T)/dT$ surface taken from a GaAs solar cell in Fig. 1(a). The defect signature appears as a ridge in $dC(\omega, T)/dT$. The temperature derivative method slices the $dC(\omega, T)/dT$ surface at a fixed ω along the T axis [indicated by the arrow in Fig. 1(a)] to arrive at a dC/dT versus T curve. Similarly, the frequency derivative method slices the $\omega dC(\omega, T)/d\omega$ surface [Fig. 1(b)] at a fixed T along the ω axis to arrive at a $\omega dC/d\omega$ versus ω curve. Figure 2 shows the isothermal (200 K) frequency derivative and iso-frequency (100 kHz) temperature derivative curves taken from one data set on a GaAs solar cell sample.

Figure 3 shows the Arrhenius plot of peak points obtained using the frequency derivative and temperature derivative methods; this is essentially the locus of the $dC(\omega, T)/dT$ ridge projected to the $\ln(\omega) - 1/k_B T$ plane. Both methods yield consistent activation energy and pre-exponential factor, $E_a = 268$ meV and $v_0 = 4 \times 10^{12} \text{ s}^{-1}$, demonstrating the equivalency of these two methods. In Fig. 2, the dC/dT versus T curve exhibits a peak width different from that of the $\omega dC/d\omega$ versus ω curve, which is expected because the ω axis and T axis are not directly comparable without converting both to the energy axis. We convert the T axis to E axis using Eq. (1) and v_0 obtained from the Arrhenius plot:

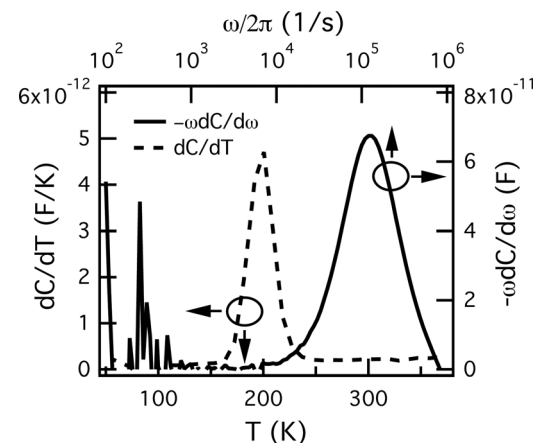


FIG. 2. Plots of $\omega dC/d\omega$ vs ω (solid) and dC/dT vs T (dashed) taken from the capacitance data of a GaAs solar cell at $\omega_{fix} = 2\pi \times 10^5$ radian/s, $T_{fix} = 200$ K, respectively.

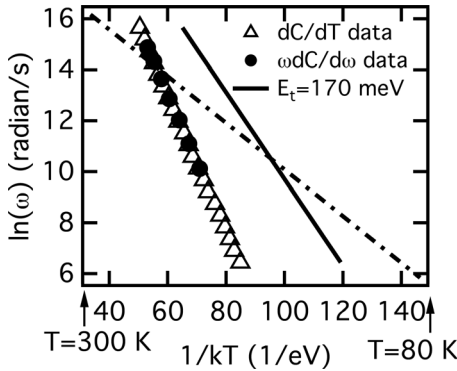


FIG. 3. The Arrhenius plots generated from peaks identified in $\omega dC/d\omega$ vs ω (solid circles) and dC/dT vs T (empty triangles) curves yielding the same activation energy and pre-exponential factor: $E_a = 268$ meV and $v_0 = 4 \times 10^{12}$ s $^{-1}$, respectively. The diagonal line (dashed line) indicates a fictitious defect which activation energy $E_{\text{diagonal}} \sim 86$ meV. For observation of defects with energy above this value, the temperature derivative method is advantageous. The Arrhenius plot of another fictitious defect with $E_a = 170$ meV is plotted (solid line) to illustrate simultaneous detection of multiple defects.

$E_\omega = k_B T [\ln(2v_0) - \ln(\omega_{\text{fix}})]$. The defect distribution in energy is determined from the temperature derivative method using Eq. (5). As seen in Fig. 4, this compares well with that from the frequency derivative method after converting the ω axis to E axis: $E_\omega = k_B T_{\text{fix}} [\ln(2v_0) - \ln(\omega)]$. Both the frequency and temperature derivative capacitance methods yield approximately the same defect density of states.

The diagonal line (dashed) in Fig. 3 shows a fictitious defect the Arrhenius plot of which extends from the highest-frequency, highest-temperature (1 MHz, 330 K) point to the lowest-frequency, lowest-temperature point (100 Hz, 80 K) of the measurable temperature-frequency range. The activation energy (~ 86 meV given the temperature and frequency limits in this particular case) of this “defect”:

$$E_{\text{diagonal}} = - \frac{\ln \omega_{\text{max}} - \ln \omega_{\text{min}}}{(k_B T_{\text{max}})^{-1} - (k_B T_{\text{min}})^{-1}} \quad (8)$$

provides a dividing point below which (that is, shallower defects) the frequency derivative method is advantageous and above which (that is, deeper defect) the temperature

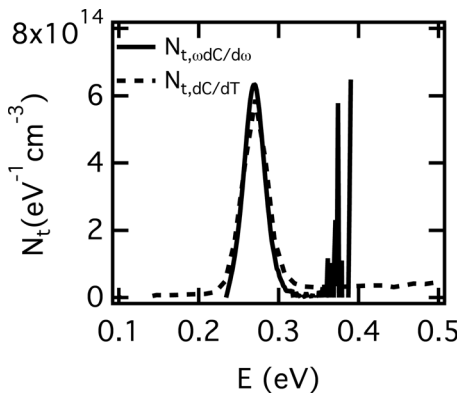


FIG. 4. The density of defect states calculated using data shown in Fig. 2 according to Eqs. (3) and (5). The density of states calculated using the temperature derivative method (dashed) agrees well with that determined from the frequency derivative method (solid).

derivative method is advantageous. This becomes clear as one visualizes in Fig. 1 the generation of the dC/dT versus T and $\omega dC/d\omega$ versus ω curves as E_a is varied. As E_a increases, that is, the line of points in the Arrhenius plot rotates clockwise toward a steeper slope, the $dC(\omega, T)/dT$ ridge rotates counter-clockwise in the $T-\omega$ plane (top down view), so that it becomes closer to normal to the T axis (or parallel to the ω axis). Therefore a greater number of distinct dC/dT versus T curves are generated as the dC/dT surface is sliced at fixed frequencies along the T axis. In contrast, fewer distinct $\omega dC/d\omega$ versus ω curves are generated by slicing at fixed temperatures along the ω axis as the ridge in the $\omega dC/d\omega$ plot rotates toward parallel with the ω axis.

Within the usable range of respective temperature and frequency ranges, and for defect energies of most interest ($> E_{\text{diagonal}}$), there are generally more data points available in the temperature derivative method to enable a higher quality Arrhenius plot and a better fitting to extract the energy and pre-exponential factor. For example, Fig. 3 shows 7 data points from frequency derivative method and 21 data points from temperature derivative method. This may not appear important in the GaAs samples studied because the density of state spectrum is very narrow. It can be important when the broadening is large as in the case of thin-film polycrystalline Cu(In,Ga)Se₂ material, for example.

B. Simulation

To quantitatively illustrate the features of these two methods, we apply them to observe a hypothetical defect with a Gaussian density of states:

$$N_t(E) = N_{t0} e^{-(E-E_a)^2/\delta E_a^2}, \quad (9)$$

where N_{t0} is the normalized density of states, E_a the peak of the Gaussian distribution, and δE_a the broadening. For the Gaussian density of states defect defined in the preceding text, the relative peak broadening of the temperature derivative dC/dT curve measured at a fixed frequency can be obtained from Eq. (1):

$$\delta T_t/T_t = \delta E_a/E_a, \quad (10)$$

where T_t is the peak temperature corresponding to E_a and $T_t \pm \delta T_t$ are the temperatures corresponding to $E_a \pm \delta E_a$. Also derived from Eq. (1), the peak broadening of frequency derivative $\omega dC/d\omega$ curve measured at a fixed temperature is

$$\delta \ln(\omega_t)/\ln(\omega_t) = \delta E_a/[k_B T_{\text{fix}} \ln(2v_0) - E_a], \quad (11)$$

where $\ln(\omega_t)$ is the natural logarithm of peak frequency corresponding to E_a and $\ln(\omega_t) \pm \delta \ln(\omega_t)$ are the natural logarithm of frequencies corresponding to $E_a \pm \delta E_a$. It is immediately obvious that the temperature derivative method has the advantage of keeping the spectral shape of the density of states, whereas the peak broadening observed by the frequency derivative method is not only different from that of the density of states but also dependent on T_{fix} , v_0 , and E_a .

Assume that a peak is recognizable when there are data measured at least δT_t [or $\delta \ln(\omega_t)$] away from either side of

the peak T_t [or $\ln(\omega_t)$]. The limits of defect energy observable by the temperature derivative method are:

$$E_{T,\min/\max} = \frac{k_B T_{\min/\max} [\ln(2v_0) - \ln(\omega_{\text{fix}})]}{1 \mp m\delta E_a/E_a}. \quad (12)$$

For the frequency derivative method, the limits of observable defect energy are:

$$E_{\omega,\min/\max} = \frac{k_B T_{\text{fix}} [\ln(2v_0) - \ln(\omega_{\max/\min})]}{1 \mp m\delta E_a/E_a}. \quad (13)$$

The minimum observable energy should be replaced by 0 if the values calculated by Eqs. (12) and (13) are negative. Both Eqs. (12) and (13) are generally applicable to any defect provided that v_0 is known.

In the following discussion, we consider two special cases to illustrate the difference in energy limits observable by the temperature and frequency derivative methods. In the first case, we choose v_0 with three fixed values 1×10^{10} , 1×10^{12} , and $1 \times 10^{14} \text{ s}^{-1}$. These values are representative of a fairly wide range of defects reported in the literature. In the second case, we assume that the pre-exponential factor, related to the capture cross-section of the defect, satisfies Meyer–Neldel’s rule:¹²

$$v_0 = v_{00} e^{E_a/k_B T_{\text{iso}}}, \quad (14)$$

where v_{00} is the normalized pre-exponential factor and T_{iso} is the iso-kinetic temperature. For data simulation of this work, we use the mean of the two sets of experimental values in Ref. 13: $T_{\text{iso}} = 440 \text{ K}$ and $v_{00} = 4 \times 10^7 \text{ s}^{-1}$. Meyer–Neldel’s rule,¹² although frequently reported in defect studies, is not universal. We choose Meyer–Neldel’s rule in the second special case so that both E_a and v_0 are allowed to vary.

In Fig. 5 we plot the maximum and minimum defect energies observable in both special cases ($\omega_{\text{fix}} = 2\pi \times 10^2 \sim 10^6 \text{ radian/s}$, $T_{\text{fix}} = 80 \sim 330 \text{ K}$). The energy window observable by the temperature derivative method is typically larger than that of the frequency derivative method for both special cases evaluated (for example, at $\omega_{\text{fix}} = 5 \times 10^4 \text{ radian/s}$, a Meyer–Neldel’s rule-obeying defect between ~ 0.1 and 0.7 eV is observable by the temperature derivative method compared to ~ 0.1 – 0.4 eV by the frequency derivative method at $T_{\text{fix}} = 200 \text{ K}$). Due to the narrower observable energy window using the frequency derivative method, a single defect may escape detection in certain temperature ranges. Also, if there are multiple defects sparsely located at different energies, they may not be seen at the same temperature. Owing to its wider observable energy range, the temperature derivative method enables higher detection probability for single defects and simultaneous observation of multiple defects; this is clearly advantageous if the defect location and number of defects are not known *a priori*. In Fig. 3, we plotted the Arrhenius plot (solid line) of a fictitious deep defect with $E_a = 170 \text{ meV}$ along side the actual experimental data to illustrate the case of simultaneous detection of multiple defects. Obviously, both deep defects can be seen simultaneously (on the same dC/dT vs T curve) at any fixed frequencies within the experimental range by the temperature

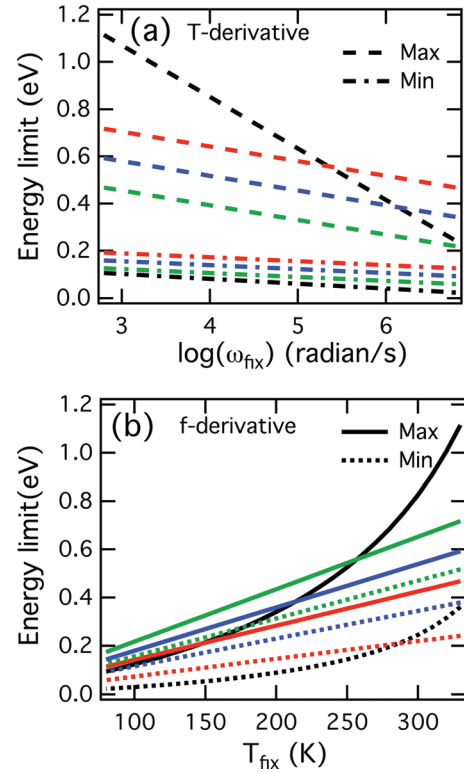


FIG. 5. (Color) The limits of observable energy by (a) the temperature derivative method (maximum, dashed line; minimum, dash-dotted line) and (b) the frequency derivative method (maximum, solid line; minimum, dotted line), calculated according to Eqs. (12) and (13), respectively. The color scheme is used to distinguish the different simulation settings: E_a and v_0 obeying Meyer–Neldel’s rule (black), fixed $v_0 = 1 \times 10^{10} \text{ s}^{-1}$ (red), fixed $v_0 = 1 \times 10^{12} \text{ s}^{-1}$ (blue), and fixed $v_0 = 1 \times 10^{14} \text{ s}^{-1}$ (green). The temperature derivative method generally allows a wider window of observable energy within the same ranges of frequency (0.1–1000 kHz) and temperature (80–300 K).

derivative method. Using the frequency derivative method, however, they can only be seen simultaneously (on the same $\omega dC/d\omega$ vs ω curve) at fixed temperatures between 135 and 180 K (that is, $65 < 1/k_B T < 85 \text{ eV}^{-1}$ in Fig. 3) which is only a small portion of the entire measured temperature range.

The actual capacitance measurement consists of contributions from other factors such as intrinsic device parasitic parameters, extrinsic measurement circuit effects, etc. The extrinsic effects such as series resistance of contacts and cables and parasitic inductance are sensitive to frequency change and can easily mix with the intrinsic junction capacitance and conductance, appearing as a baseline or background in the $\omega dC/d\omega$ versus ω curve. Therefore, one often faces the need of discerning and excluding such frequency-dependent effects from the frequency derivative method. This is difficult at times and may require complicated circuit analysis and decomposition methods. The aforementioned extrinsic effects are, however, usually no more sensitive to temperature variation than the junction capacitance and conductance. Indeed if these effects originated from locations outside of cryostat, they should not exhibit any temperature dependence at all. This means that the temperature derivative method is inherently more immune to such extrinsic effects that are frequency sensitive.

Noise at the low frequency end is always present in frequency derivative method, as can be seen in Fig. 2, which means that usually only the high frequency half of the $\omega dC/d\omega$ spectrum is useful at any temperature. This makes it difficult to identify the peak when whole peak fitting algorithms are used. The dC/dT spectrum is also affected by the same noise but in a different way. If the dC/dT spectrum is measured at low frequency, then the entire spectrum is affected by the noise, sometimes rendering it entirely not useful for further analysis. If dC/dT is measured at a fixed frequency from the cleaner high frequency end, then the entire dC/dT spectrum can have high signal-to-noise ratio. This difference suggests that as long as the dC/dT spectrum is measured at a suitable frequency, the peak identification and overall measurement quality is higher than the frequency derivative method.

V. CONCLUSIONS

In summary, we use the temperature derivative admittance spectroscopy technique to study the defect density of states. The quantity dC/dT is found to be proportional to the defect density of states. We compare the performance of temperature and frequency methods under practical experiment settings. Although fundamentally equivalent to the frequency derivative methods due to the temperature-rate duality, the temperature derivative method is found superior in several aspects. We define the activation energy of a fictitious defect the Arrhenius plot of which extends diagonally across the measurable temperature-frequency range, below which (that is, shallower defects) the frequency derivative method is advantageous and above which (that is, deeper

defect) the temperature derivative method is advantageous. In two special but representative cases simulated, the temperature derivative capacitance method exhibits a wider observable energy range, allows easier observation of single or multiple defects, and produces more data points for the Arrhenius plot to enable better line fitting so that the activation energy and the pre-exponential factor can be more accurately determined. In general, the temperature derivative method is also more immune to certain background influence and low frequency noise.

ACKNOWLEDGMENTS

The authors thank Dr. A. Ptak for GaAs samples.

- ¹D. L. Losee, *J. Appl. Phys.* **46**, 2204 (1975).
- ²S. S. Hegedus and W. N. Shafarman, *Prog. Photovoltaics* **12**, 155 (2004).
- ³T. Walter, R. Herberholz, C. Muller, and H. W. Schock, *J. Appl. Phys.* **80**, 4411 (1996).
- ⁴C. Tan and M. Xu, *Solid-State Electron.* **32**, 25 (1989).
- ⁵C. Leon, J. M. Martin, J. Santamaría, J. Skarp, G. Gonzalez-Diaz, and F. Sanchez-Quesada, *J. Appl. Phys.* **79**, 7830 (1996).
- ⁶J. D. Cohen and D. V. Lang, *Phys. Rev. B* **25**, 5321 (1982).
- ⁷J. Barbolla, S. Duenas, and L. Bailon, *Solid-State Electron.* **35**, 285 (1992).
- ⁸S. Agarwal, Y. N. Mohapatra, and V. A. Singh, *J. Appl. Phys.* **77**, 3155 (1995).
- ⁹J. V. Li, S. W. Johnston, Y. Yan, and D. H. Levi, *Rev. Sci. Instrum.* **81**, 033910 (2010).
- ¹⁰*Impedance Measurement Handbook* (Agilent Technologies, Santa Clara, California, 2006).
- ¹¹J. H. Scofield, *Sol. Ener. Mater. Sol. Cells* **37**, 217 (1995).
- ¹²A. Yelon, B. Movaghfar, and R. S. Crandall, *Rep. Prog. Phys.* **69**, 1145 (2006).
- ¹³R. Herberholz, T. Walter, C. Muller, T. Friedlmeier, H. Schock, M. Saad, M. Ch. Lux-Steiner, and V. Alberts, *Appl. Phys. Lett.* **69**, 2888 (1996).